Surface studies of crystalline and amorphous Zn–In–Sn–O transparent conducting oxides

Diana E. Proffit [a,*], Steven P. Harvey [a], Andreas Klein [b], Robert Schafranek [b], Jonathan D. Emery [a], D. Bruce Buchholz [a], Robert P.H. Chang [a], Michael J. Bedzyk [a], Thomas O. Mason [a]

[a] Northwestern University, Dept. of Materials Science and Engineering, 2220 Campus Drive, Evanston, IL 60208, USA
[b] Darmstadt University of Technology, Institute of Materials Science, Petersenstrasse 23, 64287 Darmstadt, Germany

ARTICLE INFO

ABSTRACT

X-ray and ultraviolet photoelectron spectroscopy (UPS) studies were made of in situ RF magnetron-sputtered crystalline (c) and amorphous (a) Zn–In–Sn–O (ZITO) thin films, ex situ pulsed laser deposited c- and a-ZITO thin films, and bulk ZITO ceramics. Cosubstitution of Zn and Sn for In results in an increase of the In core level binding energy at a given Fermi level compared to that measured in undoped and Sn-doped In_2O_3 (ITO). In plots of work function vs. Fermi level, in situ c-ZITO and a-ZITO films have low ionization potentials (7.0–7.7 eV) that are similar to undoped In_2O_3. In contrast, dry-air-annealed in situ films, ex situ films, and bulk ceramics have higher ionization potentials (7.7–8.1 eV) that are more similar to ITO and match well with previous work on air-exposed surfaces. Kelvin Probe measurements were made of select a-ZITO films exposed to air and ultraviolet/ozone-treated so as to measure work functions under conditions commonly employed for device fabrication. Results (4.8–5.3 eV) were in good agreement with the UPS work functions of oxygen-exposed materials and with literature values. Lastly, a parallelogram plot of work function vs. Fermi level shows that a wider range of work functions is achievable in ZITO materials as compared to other transparent conducting oxides (Sb-doped SnO_2, Al-doped ZnO, Sn-doped In_2O_3), making ZITO more versatile for applications.

© 2012 Elsevier B.V. All rights reserved.

1. Introduction

Transparent conducting oxides (TCOs) are employed as transparent electrodes in flat-panel displays, electrochromic windows, light-emitting diodes (LEDs), photovoltaics (PVs) and flexible electronics [1,2]. Electronic surface potentials (Fermi level, work function) of TCOs play an especially significant role in organic-based devices such as organic LEDs and PVs because they determine the barrier height for carrier injection/extraction [3–6]. Indium tin oxide (ITO) is used in most organic-based devices, largely owing to commercial availability. However, there are drawbacks to ITO, including: 1) chemical instability (ITO is easily etched by poly(3,4-ethylenedioxythiophene) poly(styrenesulfonate), known as PEDOT:PSS [7]), 2) relatively low-temperature crystallization of amorphous ITO (crystallization of amorphous films can occur below 200 °C [8,9]), 3) the inhomogeneity of surface properties of crystalline (c-)ITO films resulting in "hot" and "dead" spots on the surface of c-ITO electrodes [5,10], and 4) the volatility of indium prices.

Since the discovery of the extended bixbyite (In_2O_3) solid solution in the Zn–In–Sn–O system [11,12], i.e., cosubstitution of In by equal amounts of Zn and Sn, as shown schematically in Fig. 1, there has been considerable interest in Zn–In–Sn–O or so-called ZITO materials. In addition to their reduced indium contents, crystalline (c-)ZITO electrodes were shown to have superior stability against PEDOT:PSS [7], and conductivities of pulsed laser-deposited (PLD) c-ZITO films were shown to be competitive with those of similarly deposited c-ITO films [13].

In addition, there are added benefits of amorphous (a-)ZITO. By PLD, we have been able to make a-ZITO TCOs with up to 70% of the In replaced by Zn/Sn, as shown schematically in Fig. 1. The benefits of a-ZITO include: 1) enhanced chemical stability (as mentioned previously), 2) improved thermal stability (in our work, a-ZITO30, with 30% of the In substituted by Zn/Sn, does not crystallize until just above 300 °C and a-ZITO70 is stable against crystallization to at least 600 °C), 3) low temperature deposition, compatible with flexible/polymer substrates, 4) sub-nanometer smooth surfaces [14–16], and 5) the potential for improved bulk and surface homogeneity (both in terms of chemical composition and electrical properties) as a result of the amorphous structure.

To date, however, little has been published regarding the electronic surface potentials (Fermi level, work function) of c-ZITO or a-ZITO materials. The present work was undertaken to fill this

* Corresponding author at: Department of Materials Science & Engineering, Northwestern University, 2220 Campus Dr., Evanston, IL 60201, USA. Tel.: +1 847 491 5286; fax: +1 847 491 7820.
E-mail address: diana.proffit@gmail.com (D.E. Proffit).
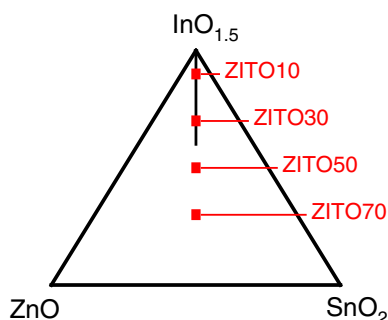
Fig. 1. Schematic diagram of the $InO_{1.5}$–SnO_2–ZnO ternary phase diagram showing the $In_{2-2x}Sn_xZn_xO_3$ ($x \leq 0.4$) solid solution and pinpointing cosubstitution levels studied in this paper (ZITO#, where # is the percent of In replaced by roughly equal amounts of Sn and Zn).

gap experimentally, and to draw useful comparisons to the literature data for In_2O_3 and ITO. Electrical and optical properties of these materials are discussed elsewhere [17,18].

The work function of a material is affected by two independent quantities: (i) the Fermi level position relative to the band edges, and (ii) the surface dipole, as shown in the schematic diagram of Fig. 2. If the Fermi level is raised through donor-doping (ΔE_F), there is a corresponding decrease in the work function (WF). However, if the atomic arrangement at the surface is modified by different surface terminations (oxygen vs. cation termination) and/or surface orientation, there can be a change in the surface dipole, leading to a change in the electron affinity (ΔEA) and the ionization potential (ΔI_P). In general, a negative surface charge causes an increase of the surface dipole and vice versa. In addition, electronegative or electropositive adsorbates can also alter the surface dipole.

To discriminate between these two contributions to the work function (Fermi level position, change in surface dipole) we employed photoelectron spectroscopy [19]. Both X-ray photoelectron spectroscopy (XPS) and ultraviolet photoelectron spectroscopy (UPS) allow the determination of the Fermi level with respect to the band edges at the surface. In addition, UPS allows the determination of the work function at a given surface. Because XPS and UPS are ultrahigh vacuum measurements, we also employed Kelvin Probe to establish work functions of select a-ZITO films exposed to air and ultraviolet (UV)/ozone treatments, as these work functions are of interest for devices in which the a-ZITO electrode has been exposed to air [20].

2. Experimental details

In situ film synthesis and all photoelectron surface analysis were carried out in the Darmstadt Integrated System for Materials Research (DAISY-MAT, TU-Darmstadt, Germany). This integrated system connects a Physical Electronics PHI 5700 multi-technique surface analysis system (Physical Electronics, Chanhassen, MN, USA) with several
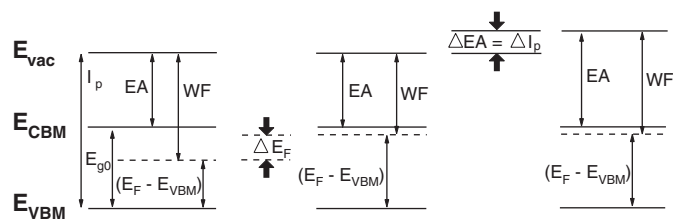
Fig. 2. Schematic diagram of the effect of changes in Fermi level position (E_F–E_{VBM}) and electron affinity (EA)/ionization potential (I_P) on work function (WF). The energy level of vacuum (E_{vac}), the conduction band minimum (E_{CBM}), and the valence band maximum (E_{VBM}) are noted. Also, the intrinsic bandgap (E_{g0}) is defined.

specimen preparation chambers by a high vacuum transfer apparatus [21].

XPS was performed using a monochromatic Al K_α radiation source with an energy resolution better than 400 meV as determined by the Gaussian broadening of the Fermi edge of a sputter-cleaned Ag standard. UPS was performed using a helium (He–I) gas discharge lamp with an excitation energy of 21.22 eV and an energy resolution better than 200 meV.

Thin films of crystalline $In_{1.8}Sn_{0.10}Zn_{0.10}O_3$ (ZITO10) and $In_{1.4}Sn_{0.30}Zn_{0.30}O_3$ (ZITO30) were deposited in the DAISY-MAT by RF magnetron sputtering using 2 in. (diameter) ceramic targets (Mateck GmbH, Jülich, Germany). Sputtering was performed for 1 h under 0.5 Pa of either pure argon or a 90% Ar–10% O_2 mixture, a power of 25 W, a gas flow rate of 20 sccm, a target-to-substrate distance of 8.4 cm, and a substrate temperature of 220 °C. Films were deposited on commercial ITO coated glass substrates (Merck Inc., Whitehouse Station, NJ) to prevent binding energy shifts during UPS measurements due to charging effects in less conductive films.

For the abovementioned films deposited under pure argon, subsequent annealing treatments were performed following initial analysis without breaking vacuum. First the films were subjected to an oxidation anneal under 0.5 Pa O_2. The ZITO30 films were annealed at 400 °C for 8 h and ZITO10 films were annealed at 500 °C for 2 h. After a second analysis, the films were subjected to a reduction anneal at 0.5 Pa H_2. The ZITO30 films were annealed at 400 °C for 7–12 h or 500 °C for 2 h and the ZITO10 films were annealed at 500 °C for 2 h. In all cases the samples were cooled in the annealing atmosphere at the natural system cooling rate (~1 h to reach room temperature). The films grown and treated solely in the DAISY-MAT system comprise the in situ c-ZITO thin film dataset, as photoelectron spectroscopy was performed without breaking vacuum after deposition and treatment.

A small subset of the in situ deposited ZITO10 thin films were subjected to subsequent dry air annealing outside of the DAISY-MAT system. These films were annealed in a fused quartz tube at 450 °C for 48 h under a flow of dry air from a compressed gas cylinder. Heating and cooling were performed at 3 °C/min. After re-loading these samples in the DAISY-MAT system, analysis was carried out on the as-annealed films. Then an oxidation anneal (0.5 Pa O_2, 500 °C, 2 h) and a reduction anneal (0.5 Pa H_2, 500 °C, 2 h) were performed, followed each time by XPS/UPS analyses. This set of data is referred to as the air-annealed in situ c-ZITO10 thin films.

In addition, thin films of a-ZITO30 and $InSn_{0.50}Zn_{0.50}O_3$ (ZITO50) were deposited by RF magnetron sputtering in the DAISY-MAT system as described above. However, the pressure ranged from 0.5 Pa to 5 Pa and the gas composition was varied between 100% argon, a 99.5% Ar–0.5% O_2 mixture, and a 99% Ar–1% O_2 mixture. The films were deposited on commercial F-doped SnO_2 coated glass substrates, which were not heated during deposition. These films comprise the in situ a-ZITO thin film dataset.

Additional thin films of c-ZITO30 and amorphous $In_{0.6}Sn_{0.70}Zn_{0.70}O_3$ (ZITO70) were deposited outside the DAISY-MAT via PLD. A 248 nm KrF Excimer laser with a 25 ns pulse duration was operated at 2 Hz with 200 mJ/pulse incident upon a 1 inch ceramic target. The target was rotated at 5 rpm and the laser beam was rastered to prevent localized heating of the target. The c-ZITO30 thin films were deposited on (111) oriented yttria stabilized zirconia at 700 °C with a deposition ambient of 4.0 and 10.0 Pa. The a-ZITO70 thin film was deposited on glass without heating the substrate at a deposition ambient of 1.0 Pa of oxygen.

Owing to the breaking of vacuum between deposition and analysis, removal of carbon contamination was necessary. For both sets of PLD films, oxidation and reduction anneals were performed, followed each time by XPS/UPS analysis. First an oxidation anneal was performed under 0.5 Pa O_2 for 2 h at 450 °C. After analysis, a subsequent reduction anneal was done under vacuum (ranging

from 10^{-5} to 10^{-6} Pa) for 2 h at 450 °C. For the c-ZITO30 films, a second reduction anneal was completed under 0.5 Pa H$_2$ for 2 h at 450 °C. Alternatively, an additional oxidation anneal was completed on the ZITO70 film between the first oxidation anneal and the reduction anneal because UPS analysis was not possible after the first oxidation anneal. This additional oxidation anneal was completed under 0.5 Pa O$_2$ for 1 h at 400 °C. These sets of data comprise the ex situ c-ZITO30 and the ex situ a-ZITO70 thin film datasets, respectively.

Finally, bulk ceramic samples of ZITO15 (In$_{1.7}$Sn$_{0.15}$Zn$_{0.15}$O$_3$), ZITO30, and ZITO40 (In$_{1.2}$Sn$_{0.4}$Zn$_{0.4}$O$_3$) specimens were prepared by conventional solid state reaction methods in air with additional care to minimize the vaporization of zinc during sintering as detailed elsewhere [13]. Upon introduction to the DAISY-MAT system, these samples were also subjected to an oxidation anneal (450 °C, 2 h, 0.5 Pa O$_2$) and a reduction anneal (450 °C, 2 h, 10^{-5}–10^{-6} Pa vacuum), with XPS/UPS analyses at each step.

For all samples, crystallinity and phase composition were checked using either general X-ray diffraction (XRD — bulk samples) and/or grazing incidence X-ray wide angle scattering (GIWAXS — thin films). For XRD of bulk samples, a Rigaku Dmax diffractometer (Tokyo, Japan) with a Cu K$_\alpha$ source was used. GIWAXS of thin film samples were performed at the Dupont-Northwestern-Dow Collaborative Access Team (DND-CAT) beamline 5-ID-C at Argonne National Laboratory's Advanced Photon Source. These data were obtained using 17.00 keV X-rays and a Mar 165 area detector located ~300 mm from the sample position. X-rays impinged upon the sample at an incident angle slightly below the critical angle for ZITO, limiting the penetration depth of the X-rays to the top few nanometers of the film. Also, to further elucidate the preferred orientation of crystallites within the films, 1D azimuthal plots were extracted using the Nika software package in Igor Pro [22].

Further surface analysis was performed on the a-ZITO thin films with UPS Fermi levels close to 2.9 eV using a non-scanning ambient Kelvin probe (KP) system (KP Technology, Inc., Wick, Scotland) with a 2 mm diameter gold-coated probe head. The probe tip work function was calibrated using a gold standard. The probe-sample distance was held constant for all samples to minimize capacitive errors. Room humidity was maintained below 45% for all measurements to minimize water adsorption effects. Also, the thin film surfaces were grounded using aluminum tape. Prior to KP measurement, the films were cleaned by rinsing multiple times under ethanol, acetone, hexane, and deionized water, were subsequently dried by nitrogen gas spray (following an ethanol rinse), and then subjected to an UV/ozone treatment. The a-ZITO30 film was treated for 10 min and the a-ZITO50 and a-ZITO70 films were treated for 15 min.

3. Results and discussion

XPS and UPS spectra, including both surveys (a,b) and XPS core level spectra from the In 3d (c), Sn 3d (d), and Zn 2p (e) energy levels are shown in Fig. 3 for the a-ZITO50 film grown on ITO-coated glass with 100% Ar at 5 Pa. Dotted lines denote the core level binding energies and aid in the observation of peak symmetry. These spectra are generally representative of all ZITO films, whether amorphous or crystalline, although energy shifts are observed that will be discussed later in more detail. The XPS survey spectrum contains only emission peaks for In, Sn, Zn, and O, confirming the composition of the films. ZITO50 films exhibit higher Sn and Zn peaks and lower In peaks compared to ZITO30 films, which corresponds with expected changes in composition. The UPS survey spectrum shows a sharp secondary electron cutoff that is necessary for calculating work functions.

The In-3d$_{5/2}$ core level binding energy vs. Fermi level (relative to the valence band maximum) is plotted for all the crystalline specimens in Fig. 4a, with the inset diagram showing an enlargement of the congested region around E$_F$ = 2.8 eV. The solid line has a slope of one, corresponding to parallel shifts of the In-3d$_{5/2}$ core level binding energy and the Fermi level owing to donor doping. For comparison purposes, data from our prior work on In$_2$O$_3$ and ITO are represented by the dashed line [23,24]. There is a noticeable shift of the line (with slope equal to one) for all c-ZITO specimens vs. that for the c-ITO data. The larger binding energy of the In 3d core level with respect to the valence band maximum in ZITO as compared to ITO might be related to a reduced screening of the photoemission final state [25]. All of the data for the c-ZITO films and bulk specimens tend to fall on or near the solid line regardless of cosubstitution level, i.e., the presence of Zn/Sn as opposed to
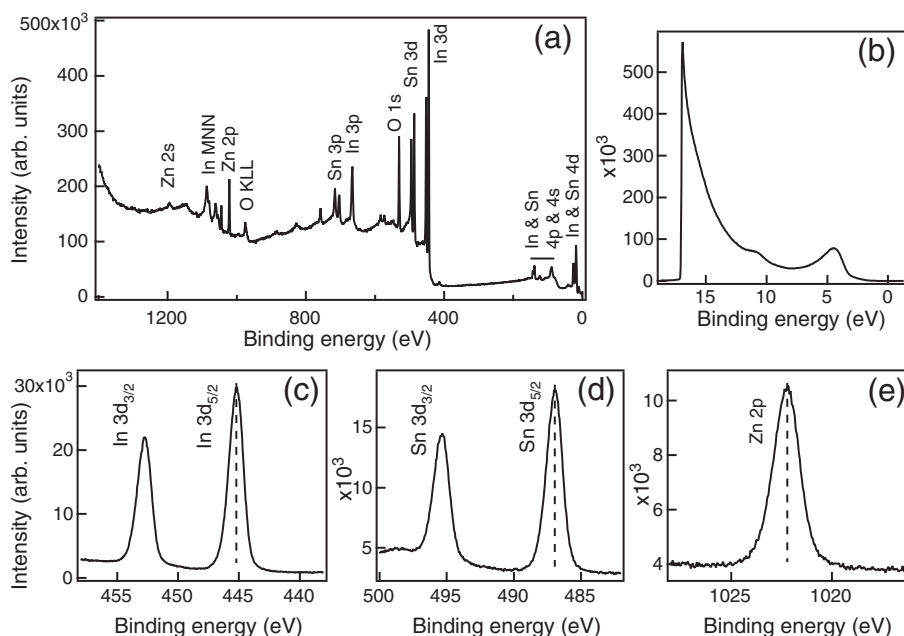
Fig. 3. XPS and UPS spectra, including the (a) XPS survey spectrum, (b) UPS survey spectrum, and core level spectra ((c) In 3d, (d) Sn 3d, (e) Zn 2p), for the a-ZITO50 film deposited on ITO-coated glass with 100% Ar at 5 Pa. These spectra give E$_F$(XPS) = 2.93 eV, E$_F$(UPS) = 3.08 eV, WF = 4.22 eV, and IP = 7.30 eV.
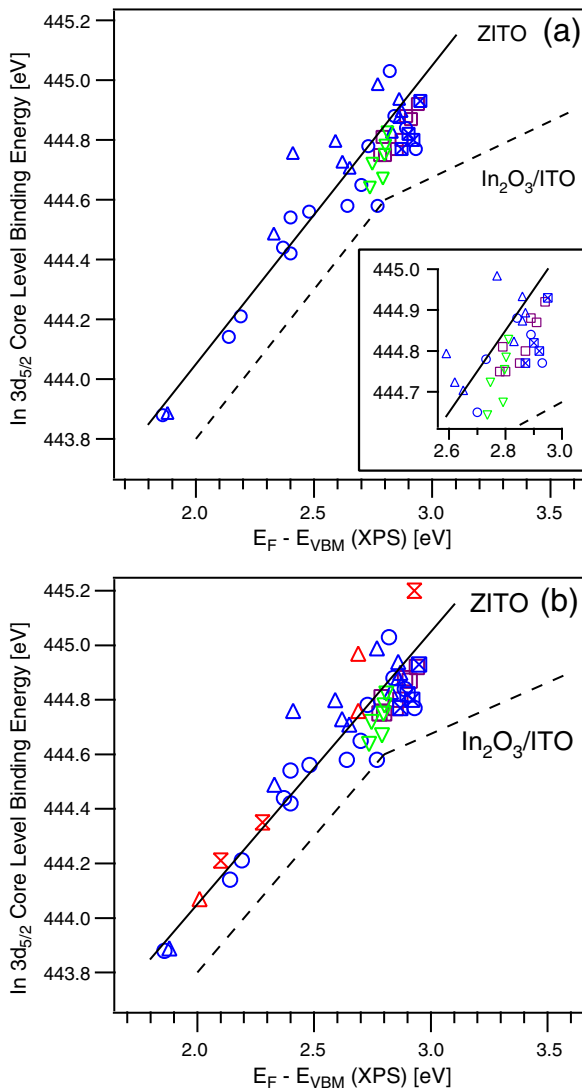
Fig. 4. In $3d_{5/2}$ core level binding energy vs. Fermi level position for (a) crystalline ZITO specimens and (b) amorphous ZITO specimens superimposed on crystalline ZITO specimens. The individual data are: bulk c-ZITO ceramics (purple squares), in situ c-ZITO10 thin films (blue circles), in situ c-ZITO30 thin films (blue triangles), air-annealed in situ c-ZITO10 thin films (blue crossed squares), ex situ c-ZITO30 thin films (green inverted triangles), in situ a-ZITO30 thin films (red triangles), and in situ a-ZITO50 thin films (vertical bowties). All in situ thin films are grown via RF magnetron sputtering and all ex situ thin films are grown via pulsed laser deposition. The solid black line represents a slope of one for ZITO. The dashed black line represents a slope of one for In_2O_3 and ITO, along with the accompanying deviation from this slope at high Fermi levels due to degenerate doping and screening effects.

attributable to insufficient doping, i.e., too few electrons lying above the conduction band edge in the c-ZITO specimens, but often these materials exhibit carrier concentrations similar to those in ITO. Alternatively, it may be that screening efficiencies in ZITO are lower than in ITO as a result of the additional Zn 4s and Sn 5s orbital contributions to the conduction band minimum. An irregular distribution of Zn and Sn would further decrease screening efficiencies due to local variations in the conduction band minimum and a resulting higher localization of the conduction band states. Reduced screening of the In 3d core level is further suggested by the absence of plasmon satellites (seen as asymmetry), which are correlated to screening by conduction electrons [29].

Fig. 4b shows that the a-ZITO thin film data fall roughly on the same trend line of In-$3d_{5/2}$ core level binding energy vs. Fermi level as the c-ZITO data, indicative of a similar parallel shift of In-$3d_{5/2}$ core level binding energy and Fermi level with doping. It is interesting to note that the XPS Fermi level range for a-ZITO films is approximately the same as that of the c-ZITO materials (thin film, bulk) or ~2.0–3.0 eV. Although optical measurements on a-ZITO30 thin films exhibit a bandgap similar to c-In_2O_3 and c-ZITO (~2.8 eV) [29], again no "kink" is observed in the In-$3d_{5/2}$ core level binding energy vs. Fermi level data. This could similarly be attributed to insufficient doping, i.e., too few electrons lying above the conduction band edge, but again the carrier concentrations in these films are often similar to those seen in their crystalline counterparts [18]. However, it should be noted that the a-ZITO50 film with a Fermi level position of 2.9 eV did not exhibit metal-like emissions at the Fermi edge in UPS spectra, as did the c-ZITO films. As exemplified in Fig. 3e, the In 3d core level spectra for a-ZITO films also show no significant plasmon satellites that might indicate free electron screening. Nevertheless, conduction band variations as a result of doping and/or local structure changes cannot be ruled out as being responsible for the absence of free electron screening.

Before discussing the work function vs. Fermi level results, it is helpful to review our prior data for In_2O_3 and ITO [19,23,24]. As shown schematically in Fig. 5, our prior In_2O_3 data are roughly bounded by constant ionization potential lines of 7.0 eV and 7.7 eV. The most stable surface for In_2O_3 is the (111) surface, which has an

cosubstitution level seems to be responsible for the shift. There is no "kink" detected in the c-ZITO materials up to $E_F(XPS) = 3.0$ eV. The kink in the ITO data for specimens doped to high Fermi levels (~3.5 eV) was interpreted as arising from additional screening of the photoemission core hole by free electrons in the conduction band [24]. In addition, this deviation from linearity in ITO was accompanied by the appearance of metal-like emissions at the Fermi edge in UPS spectra (for E_F ~ 2.9 eV or greater). It was concluded that the band gap of In_2O_3/ITO is ~2.8 ± 0.2 eV, consistent with other experimental/theoretical findings [26,27]. We hasten to add that Fermi edge emissions were consistently observed in our in situ c-ZITO10 and c-ZITO30 films for $E_F(UPS) \geq 2.8$ eV [28]. This suggests that the band gaps of at least the c-ZITO10 and c-ZITO30 materials are roughly identical to that of ITO. The lack of a "kink" might be

Fig. 5. Work function vs. Fermi level position for In_2O_3 and ITO. The left side of each parallelogram corresponds to the minimum Fermi level position observed, the right side of the parallelogram corresponds to the maximum Burstein–Moss shift observed, and the top and bottom lines correspond to ranges in ionization potential. The solid black lines denote constant ionization potential lines of 7.0 eV, 7.7 eV, and 8.1 eV.

ionization potential of 7.0 eV as confirmed by both first principles theory and UPS measurements on epitaxial thin films [30,31]. Data for bulk ceramics and dry-air-annealed thin films fall close to the 7.7 eV ionization potential line. The rationale for an ionization potential of 7.7 eV in air-exposed samples is unclear at the present time. However, it should be noted that a peroxide (oxygen dimer)-stabilized epitaxial (100) In_2O_3 surface was recently shown to exhibit an ionization potential of 7.7 eV [30].

In contrast, in situ ITO thin film data tend to cluster on or near the 7.7 ionization potential line, consistent with the preference of ITO films to grow with (100) orientation [31], whereas data for bulk ceramic specimens or dry-air-annealed thin film specimens approach or fall on the 8.1 eV ionization potential line [13]. Again, the rationale for the higher (8.1 eV) ionization potential is unclear at the present time. However, the rationale for the presence of the (100) orientation in ITO versus the (111) orientation in In_2O_3 is better understood. Ágoston and Albe [31] have proposed that the addition of Sn dopants destabilizes surface peroxides at high Fermi levels. They state that a higher electron concentration due to higher Sn-doping levels and/or Sn segregation to the surface can cause the surface energy of the (100) surface to fall below that of the (111) surface.

We now consider the c-ZITO results in Fig. 6a. The data for in situ c-ZITO10 and c-ZITO30 thin films fall on or near the 7.0 eV ionization potential line, resembling pure In_2O_3. This remains true regardless of in situ oxidation/reduction treatments; these films maintain a roughly constant ionization potential under all conditions studied. It should be noted that the film compositions match well to the target compositions, indicating surface segregation plays little-to-no role in ionization potential variations. By GIWAXS, the in situ c-ZITO10 and c-ZITO30 films were confirmed to be mostly polycrystalline with a slight inclination of (100) surface texturing, likely derived from the slight (100) texture of the ITO substrate coating. Nevertheless, it is unlikely that the small degree of (100) texture will dominate the surface properties. Instead, the (111) surfaces should dominate, since they have the lowest work function at a particular Fermi level position (i.e., the lowest ionization potential). The (111) surface is relatively chemically inert and maintains its stoichiometry across a broad range of oxygen chemical potentials [31]. This may account for the unchanging ionization potential with post-deposition-annealing of the in situ c-ZITO films.

Upon ex situ dry-air-annealing of in situ c-ZITO10 films or measurement of ex situ c-ZITO30 films, the work function data rise considerably, falling roughly between the 7.7 eV and 8.1 eV ionization potential lines, resembling ITO. The bulk ceramic data similarly fall in this range. Both the dry-air-annealed films and bulk ceramic data are consistent with our prior work on Al-doped ZnO (AZO), Sb-doped SnO_2 (ATO), and ITO showing that the work function vs. Fermi level data for ceramic specimens and dry-air-annealed films always tend toward the high extreme of ionization potential for each system [19]. In fact, a rise in ionization potential is a persistent symptom of exposure to air (at high temperatures) or ozone in In_2O_3, ITO, and ZITO specimens.

As with ITO, the exact origin of this rise in ionization potential with high temperature air exposure is not well understood, but it is known that the (100) and (211) surfaces in In_2O_3 will form partial or full peroxides on the surface at high oxygen chemical potentials, leading to significant increases of ionization potential [31]. In addition, the adsorption of water and other species can also influence the surface dipole (and ionization potential). We would argue that the increase in ionization potential may be directly related to the oxygen environments to which the ZITO specimens are exposed. The mid-range ionization potential specimens (7.7 eV – ex situ c-ZITO30) were exposed to air only at room temperature, whereas the highest ionization potential specimens (8.1 eV – bulk c-ZITO) were sintered in air at high temperature (1275 °C). The surface texture may or may not play a role; the ex situ c-ZITO30 films had a slight
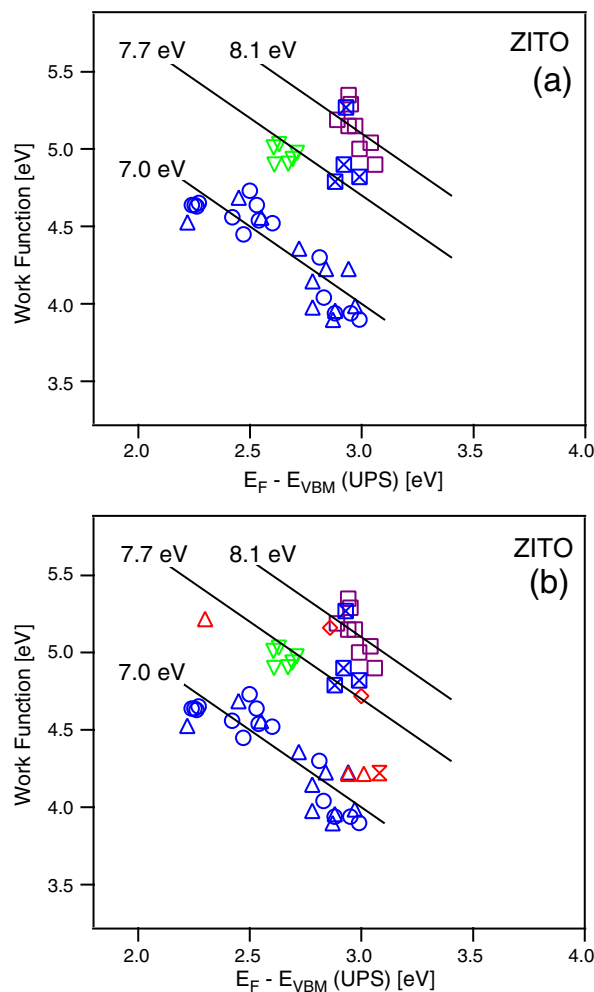
Fig. 6. Work function vs. Fermi level position for (a) crystalline ZITO specimens and (b) amorphous ZITO specimens superimposed on crystalline ZITO specimens. The individual data are: bulk c-ZITO (purple squares), in situ c-ZITO10 thin films (blue circles), in situ c-ZITO30 thin films (blue triangles), air-annealed in situ c-ZITO10 thin films (blue crossed squares), ex situ c-ZITO30 thin films (green inverted triangles), in situ a-ZITO30 thin films (red triangles), in situ a-ZITO50 thin films (vertical bowtie), and ex situ a-ZITO70 thin films (red diamonds). All in situ thin films are grown via RF magnetron sputtering and all ex situ thin films are grown via pulsed laser deposition. Constant ionization potential lines of 7.0 eV, 7.7 eV, and 8.1 eV are given by black lines.

(111) texture whereas the in situ c-ZITO10 films had a slight (100) texture. The role of surface texture can only be resolved by careful studies of epitaxial ITO and ZITO surfaces.

Overall, the present work demonstrates that c-ZITO is more versatile than c-ITO with regard to the range of work functions achievable at a fixed Fermi level. As can be seen in Fig. 6, c-ZITO can be prepared with work functions ranging from 3.9 eV to 5.4 eV at a Fermi level of 2.9 eV. In contrast, in c-ITO with $E_F = 2.9$ eV, work functions range from 4.6 to 5.2 eV [23,24].

The a-ZITO results have been superimposed on the c-ZITO data in Fig. 6b and exhibit quite similar behavior to that of c-ZITO, including compositions that are similar to the target compositions. (The work functions of two of the in situ a-ZITO50 specimens in Fig. 4 could not be reliably determined by UPS owing to imprecise secondary electron cutoff energies.) The in situ a-ZITO30 and a-ZITO50 data fall between the 7.0 eV and 7.7 eV ionization potential lines. Furthermore, the highly doped (E_F~3.0 eV) in situ a-ZITO30 and a-ZITO50 data lie close to the 7.0 eV ionization potential line. This is

understandable, given the non-polar, stoichiometric nature of both amorphous and crystalline (111) surfaces.

The ex situ a-ZITO70 film was the only amorphous film subjected to high temperature in situ annealing (up to 450 °C) to remove carbon contamination. The other amorphous films had substantially lower crystallization temperatures (<450 °C), and fortunately did not require carbon removal. The work function vs. Fermi level (UPS) data for the annealed a-ZITO70 film fall between the significantly higher 7.7 eV and 8.1 eV ionization potential lines, which is very similar in behavior to the dry-air-annealed c-ZITO10 films, ex situ c-ZITO30 films, and the bulk ceramic specimens. Although this film was only subjected to air exposure at room temperature, this ionization potential again points to the role of air exposure – oxidation, peroxidation, and/or adsorption of other species – in increasing the ionization potential. Further work is required to identify the underlying mechanism(s).

Due to the expanding use of air-exposed a-ZITO films as electrodes in organic-based devices, we also measured the work functions of a-ZITO films with Fermi levels near 2.9 eV by ambient Kelvin Probe after cleaning and UV/ozone treatment. The KP work functions are 5.3 ± 0.1 eV for a-ZITO30, 4.7 ± 0.2 eV for a-ZITO50, and 4.8 ± 0.1 eV for a-ZITO70. These values match well with those in the literature: 5.05–5.17 eV by KP [16], and 5.08–5.22 eV [32] and 5.12 eV [33], by photoelectron spectroscopy in air (PESA). Interestingly, assuming that the Fermi levels of these films remain at the level measured by UPS after UV/ozone treatment, these work function measurements indicate the ionization potentials of these treated films fall within the set of dry-air-annealed in situ films and bulk ceramic samples. Again, exposure to air and to the highly oxidizing conditions of the UV/ozone treatment likely plays a dominate role in increasing work function in these films.

In a prior paper, we introduced a version of the parallelogram plot shown in Fig. 7 [24]. This diagram provides a practical means of comparing the various TCO systems in terms of practically achievable work functions. The left side of each parallelogram corresponds to the bandgap, since Fermi levels below the conduction band correspond to materials insufficiently doped for good TCO behavior. For ATO and AZO the right side corresponds to a Burstein–Moss shift of Fermi level by doping to ~0.5 eV above the fundamental gap [34,35]. The right boundary for ITO is 0.6 eV above the band gap, to account for the still larger Fermi level (Burstein–Moss) shifts consistently observed in thin films. For In_2O_3 and ZITO, the right side of the parallelogram is based upon experimental data in prior work [19] and the present work. It is uncertain if these two materials can be degenerately doped to significantly higher Fermi levels. For each parallelogram, the lower and upper lines correspond to the minimum and maximum experimental ionization potentials found for each system.
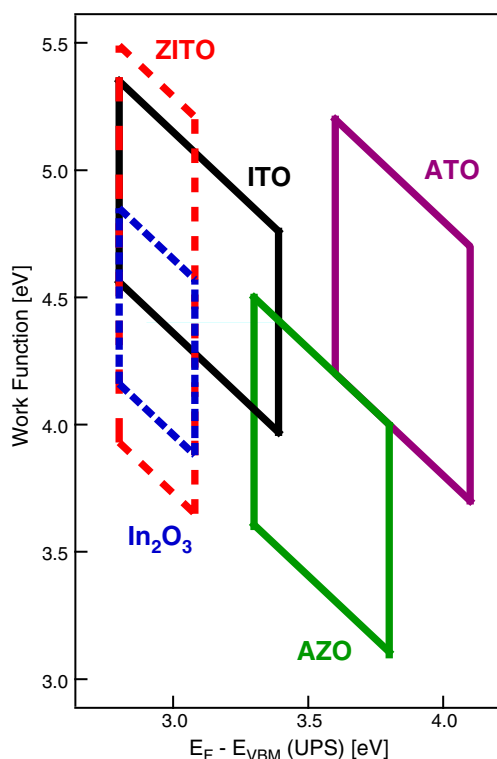
Fig. 7 suggests again that ZITO-based materials are more versatile in terms of work function than ITO-based materials as a significantly wider range of work functions can be achieved at a fixed Fermi level, ranging from the low levels associated with In_2O_3 (<4.0 eV) to the higher values associated with ITO (>5.0 eV). As a result, ZITO is an attractive candidate material for photovoltaic applications.

4. Summary and conclusions

Based upon XPS results, all the ZITO data from the present work fall on or near a single line of In-3d$_{5/2}$ core level binding energy vs. Fermi level. This is true regardless of the cosubstitution level or the form of the material (bulk, thin film, crystalline, amorphous). Compared to undoped In_2O_3 and singly-doped ITO, there is a noticeable shift with Zn/Sn cosubstitution to higher In-3d$_{5/2}$ core level binding energy at a given Fermi level with respect to the valence band maximum.

The UPS data for the crystalline ZITO materials, when plotted as work function vs. Fermi level, exhibit a range of ionization potentials. The UPS data for in situ c-ZITO films fall roughly on a constant ionization potential line of 7.0 eV, which is similar to those measured for crystalline In_2O_3. In undoped In_2O_3 this ionization potential has been attributed to a prevalent (111) non-polar surface orientation [30]. It is likely that the non-polar (111) surfaces in the in situ c-ZITO films dominate the electronic character of the surfaces, despite being polycrystalline with a very slight (100) texture. Dry-air-annealed in situ and ex situ c-ZITO films exhibit much higher ionization potentials in the 7.7–8.1 eV range, similar to what is observed for c-ITO and air-exposed specimens. As with ITO, the data for bulk ceramic specimens tend toward the high (~8.1 eV ionization potential) line. The origin of this high ionization potential is not known, but clearly results from exposure to air.

The UPS data for amorphous ZITO films, when plotted as work function vs. Fermi level, also show a similar range of ionization potentials. The UPS data for in situ a-ZITO30 and a-ZITO50 films fall between the 7.0 eV and 7.7 eV ionization potential lines, with the data at high Fermi levels (~3.0 eV) lying close to the 7.0 eV ionization potential line. This ionization potential is understandable, given the non-polar, stoichiometric nature of both amorphous and crystalline In_2O_3 (111) surfaces. On the other hand, the data for ex situ a-ZITO70, the only amorphous composition capable of undergoing post-deposition-annealing without crystallization, fall between the 7.7 eV and 8.1 eV ionization potential lines. This is consistent with the c-ZITO specimens exposed to air (dry-air-annealed in situ films, ex situ c-ZITO30 films, and bulk ceramic specimens).

The ambient KP work function measurements of the a-ZITO films also demonstrate that film exposure to air results in an increase in ionization potential (assuming that the Fermi levels in the films remain after UV/ozone treatment). The a-ZITO KP work function values ranged from 4.7 ± 0.2 eV to 5.3 ± 0.1, which match well with our air-exposed a-ZITO UPS data and also with work functions

Fig. 7. Work function vs. Fermi level position for ATO, AZO, ITO, In_2O_3, and ZITO. The left side of each parallelogram corresponds to the bandgap, the right side of the parallelogram corresponds to the maximum Burstein–Moss shift, and the top and bottom lines correspond to ranges in ionization potential.

reported in the literature. These values are promising for organic-based devices where electrode work functions greater than 5.0 eV are desired.

Finally, we have constructed parallelogram plots of achievable work function vs. Fermi level for practical TCO applications. In each case, the left boundary corresponds to the band gap, since sub-band gap Fermi levels are not associated with good TCO conductivities. The right boundary corresponds to the Burstein–Moss shift of Fermi level with doping (for ATO, AZO, and ITO) or the experimental results in our prior work for undoped In_2O_3 [19] and the present work for c-ZITO. It can be seen that ZITO is more versatile than ITO and the other basis oxides (AZO, ATO), having a wider range of achievable work functions (3.9–5.4 eV).

Acknowledgments

References

[1] D.S. Ginley, H. Hosono, D.C. Paine, Handbook of Transparent Conductors, Springer, New-York NY, 2010.
[2] A. Facchetti, T. Marks, Transparent Electronics: From Synthesis to Applications, Wiley and Sons, West Sussex UK, 2010.
[3] L.S. Hung, C.H. Chen, Mater. Sci. Eng. Rep. 39 (2002) 143.
[4] M. Eritt, C. May, K. Leo, M. Toerker, C. Tadehaus, Thin Solid Films 518 (2010) 3042.
[5] N.R. Armstrong, P.A. Veneman, E. Ratcliff, D. Placencia, M. Brumbach, Acc. Chem. Res. 42 (2009) 1748.
[6] Y.L. Gao, Mater. Sci. Eng. Rep. 68 (2010) 39.
[7] J. Ni, H. Yan, A. Wang, Y. Yang, C.L. Stern, A.W. Metz, S. Jin, L. Wang, T.J. Marks, J.R. Ireland, C.R. Kannwurf, J. Am. Chem. Soc. 127 (2005) 5613.
[8] D.C. Paine, T. Whitson, D. Janiac, R. Beresford, C.O. Yang, J. Appl. Phys. 85 (1999) 8445.
[9] H. Morikawa, M. Fujita, Thin Solid Films 359 (2000) 61.
[10] M. Brumbach, P.A. Veneman, F.S. Marrikar, T. Schulmeyer, A. Simmonds, W. Xia, P. Lee, N.R. Armstrong, Langmuir 23 (2007) 11089.
[11] G.B. Palmer, K.R. Poeppelmeier, D.D. Edwards, T. Moriga, T.O. Mason, J.L. Schindler, C.R. Kannewurf, in: R.T. Fulks, G.N. Parsons, D.E. Slobodin, T.H. Yuzurika (Eds.), Flat Panel Display Materials III, San Francisco, U.S.A., April 1 4, 1997, Materials Research Society Symposium Proceedings, 471, 1997, p. 93.
[12] S.P. Harvey, K.R. Poeppelmeier, T.O. Mason, J. Am. Ceram. Soc. 91 (2008) 3683.
[13] S.P. Harvey, T.O. Mason, D.B. Buchholz, R.P.H. Chang, C. Körber, A. Klein, J. Am. Ceram. Soc. 91 (2008) 467.
[14] J. Liu, D.B. Buchholz, R.P.H. Chang, A. Facchetti, T.J. Marks, Adv. Mater. 22 (2010) 2333.
[15] J.A. Jeong, H.K. Kim, S.I. Na, Electrochem. Solid-State Lett. 12 (2009) J80.
[16] G.S. Heo, Y. Matsumoto, I.G. Gim, J.W. Park, K.Y. Kim, T.W. Kim, Solid State Commun. 149 (2009) 1731.
[17] D.B. Buchholz, D.E. Proffit, M.D. Wisser, T.O. Mason, R.P.H. Chang, Prog. Nat. Sci. Mater. Int. 22 (2012) 1.
[18] D.B. Buchholz, J. Liu, T.J. Marks, M. Zhang, R.P.H. Chang, ACS Appl. Mater. Interfaces 1 (2009) 2147.
[19] A. Klein, C. Körber, A. Wachau, F. Säuberlich, Y. Gassenbauer, R. Schafranek, S.P. Harvey, T.O. Mason, Thin Solid Films 518 (2009) 1197.
[20] J.S. Kim, B. Lagel, E. Moons, N. Johansson, I.D. Baikie, W.R. Salaneck, R.H. Friend, F. Cacialli, Synth. Met. 111 (2000) 311.
[21] D. Ensling, A. Thissen, Y. Gassenbauer, A. Klein, W. Jaegermann, Adv. Eng. Mater. 7 (2005) 945.
[22] J. Ilavsky, J. Appl. Crystallogr. 45 (2012) 324.
[23] S.P. Harvey, T.O. Mason, Y. Gassenbauer, R. Schafranek, A. Klein, J. Phys. D: Appl. Phys. 39 (2006) 3959.
[24] A. Klein, C. Körber, A. Wachau, F. Säuberlich, Y. Gassenbauer, S.P. Harvey, D.E. Proffit, T.O. Mason, Materials 3 (2010) 4892.
[25] W.F. Egelhoff Jr., Surf. Sci. Rep. 6 (1987) 253.
[26] A. Walsh, J.L.F. Da Silva, S.H. Wei, C. Körber, A. Klein, L.F.J. Piper, A. DeMasi, K.E. Smith, G. Panaccione, P. Torelli, D.J. Payne, A. Bourlange, R.G. Egdell, Phys. Rev. Lett. 100 (2008) 167401.
[27] J.E. Medvedeva, C.L. Hettiarachchi, Phys. Rev. B 81 (2010) 125116.
[28] S.P. Harvey, Ph.D. Thesis, Northwestern University, USA, 2008.
[29] C. Körber, V. Krishnakumar, A. Klein, G. Panaccione, P. Torelli, A. Walsh, J.L.F. Da Silva, S.-H. Wei, R.G. Egdell, D.J. Payne, Phys. Rev. B 81 (2010) 165207.
[30] M.V. Hohmann, P. Ágoston, A. Wachau, T.J.M. Bayer, J. Brötz, K. Albe, A. Klein, J. Phys. Condens. Matter 23 (2011) 334203.
[31] P. Ágoston, K. Albe, Phys. Rev. B 84 (2011) 045311.
[32] C.W. Ow-Yang, H.Y. Yeom, D.C. Paine, Thin Solid Films 516 (2008) 3105.
[33] J.H. Bae, J.M. Moon, S.W. Jeong, J.J. Kim, J.W. Kang, D.G. Kim, J.K. Kim, J.W. Park, H.K. Kim, J. Electrochem. Soc. 155 (2008) J1.
[34] I. Hamberg, C.G. Granqvist, K.F. Berggren, B.E. Sernelius, L. Engström, Phys. Rev. B 30 (1984) 3240.
[35] B.E. Sernelius, K.F. Berggren, Z.C. Lin, I. Hamberg, C.G. Granqvist, Phys. Rev. B 37 (1988) 10244.